Design and experimental study of a Nonlinear Energy Sink coupled to an electromagnetic energy harvester

Giuseppe Pennisi, Brian Mann, Nicholas Naclerio, Cyrille Stephan, Guilhem Michon

To cite this version:

Giuseppe Pennisi, Brian Mann, Nicholas Naclerio, Cyrille Stephan, Guilhem Michon. Design and experimental study of a Nonlinear Energy Sink coupled to an electromagnetic energy harvester. Journal of Sound and Vibration, 2018, 437, pp.340-357. 10.1016/j.jsv.2018.08.026 . hal-04776069

HAL Id: hal-04776069
https://hal.science/hal-04776069v1

Submitted on 11 Nov 2024

Please cite this article as: G. Pennisi et al., Design and experimental study of a Nonlinear Energy Sink coupled to an electromagnetic energy harvester, Journal of Sound and Vibration (2018), https://doi.org/10.1016/j.jsv.2018.08.026

Design and experimental study of a Nonlinear Energy Sink coupled to an electromagnetic energy harvester

G. Pennisi[a,b,*], B.P. Mann[c], N. Naclerio[c], C. Stephan[a], G. Michon[b]

[a] *ONERA - The French Aerospace Lab, F-92320, Châtillon, France*
[b] *Université de Toulouse, ICA, ISAE, F-31055, Toulouse, France*
[c] *Duke University, Durham 27708, NC USA*

Abstract

Nonlinear vibration absorbers, commonly referred to as Nonlinear Energy Sinks (NESs), have been the object of several theoretical and experimental studies over the past decade. This work illustrates the theoretical design and experimental realization of a Nonlinear Energy Sink coupled to an energy harvester. The mass of the Magnetic-Strung NES is a magnet which is linked to the primary system by means of two strings with adjustable pretension that work transversally. The restoring elastic force of the strings is modulated by the magnetic force applied by two magnets suitably located on the primary mass. Either a cubic or a bistable configuration may be obtained, depending on the distance of the additional magnets, NES's efficiency as an absorber is studied on a harmonically forced single degree-of-freedom primary system. The Target Energy Transfer (TET) from the primary system to the NES, as well as different response regimes like the Strongly Modulated Response (SMR), are experimentally observed. Furthermore, the harvesting of energy from the NES vibrations is also investigated by coupling the mechanical system with a coil for electromagnetic energy conversion. Consequently, the vibration energy of the primary mass is absorbed by the NES and finally converted into electric energy.

Keywords: Nonlinear Energy Sink, Passive Vibration Control, Energy Harvesting, Targeted Energy Transfer

---

1. Introduction

A Nonlinear Energy Sink is a passive vibration absorber which is nonlinearly coupled to a primary system. The use of a Nonlinear Energy Sink (NES) as a vibration absorber has

---

[*] Corresponding author

Email addresses: `gius.pennisi@gmail.com` (G. Pennisi), `brian.mann@duke.edu` (B.P. Mann), `nicholas.naclerio@duke.edu` (N. Naclerio), `cyrille.stephan@onera.fr` (C. Stephan), `guilhem.michon@isae.fr` (G. Michon)

Preprint submitted to Journal of Sound and Vibrations. DOI: 10.1016/j.jsv.2018.08.026

been subject of interest over the last decade with studies that have shown, in comparison to the classical linear Tuned Mass Damper (TMD), that the NES could be effective over a broader frequency range and only require a small additional mass. It has been shown that the nonlinear attachments can lead to an irreversible energy transfer from the primary system towards the NES, this process is known as Targeted Energy Transfer (TET) or pumping [1, 2, 3, 4, 5]. Experimental works [6, 7, 8] have shown that the dynamics which govern this energy transfer phenomenon can be defined as a 1:1 resonance capture between the primary mass and the NES. One important and intriguing feature of a NES system is its ability to tune itself to the primary system response, since the NES does not have its own natural frequency due to its intrinsic nonlinear nature. TET under external forcing has been investigated both theoretically [9] and experimentally [10]; these studies have shown that NES systems can exhibit multiple responses of interest including steady state constant amplitude regimes and Strongly Modulated Responses (SMR). NESs have also been studied to passively control instabilities. For example, in [11] a NES is used to control the limit cycle behavior of a Van der Pol oscillator. In [12, 13, 14, 15] it was used to suppress aeroelastic instabilities. Most of the aforementioned works considered a nonlinearity with a cubic stiffness term. Fundamentally, the basic principle was to use a geometric nonlinearity of an elastic element to obtain a cubic nonlinearity in the restoring force. Nevertheless, the nature of the nonlinearity used in the NES may be of any kind. Later studies have explored other ideas such as: non-polynomial functions[16], multiple states of equilibrium [17], non-smooth functions and Vibro-Impacts [18, 19, 20, 21, 22].

Energy harvesting from the environment [23] has recently received considerable attention and many works have been motivated by advancements in the microelectronics industry, which have enabled a reduction in the power consumed by MEMS devices [24, 25]. Solar, chemical, and thermal methods have been extensively investigated and recognized as potential sources of energy. The harvesting of energy from either structural born vibrations or the motions of rigid structures has also shown much promise. Many early works considered inertial generators with linear behavior [26]. A primary limitation of linear inertial generators is their narrow-band efficacy; i.e. their performance significantly decreases for any mismatch of the excitation and resonance frequency [27]. Tuning the device's resonance and widening the bandwidth by adding many oscillators are some methods that have been studied to overcome this limitation in [28, 29].

Analogous to the vibration absorber, nonlinearity seems to also offer the potential to improve performance in energy harvesting systems. One of the first experimental investigations of an energy harvester specifically designed to exhibit a nonlinear response was described in [30] where magnetic levitation was used to extend the device bandwidth. A similar study based on piezoelectric energy conversion is presented in [31]. A piezoelectric nonlinear energy harvester is presented in [32] where high power output and wide working bandwidth are reached. The same authors have also investigated a new magnetoelectric generator in [33]. Many systems demonstrate the advantages of monostable Duffing oscillators for increased bandwidth. The bistable Duffing oscillator has also been investigated for energy harvesting in references [34, 35].

In this paper the two research fields of nonlinear vibration absorbers and energy harvesting are combined. The study of a new concept of cubic NES coupled to an electromagnetic harvester is presented. By means of a magnetic force, the nonlinear force between the NES and the primary system can be adjusted and shaped to test different configurations. Three configuration are experimentally tested and the results are compared to highlight the potential use of the device as an absorber and/or energy harvester.

2. Design of the Magnetic-Strung NES

Figure 1 shows a picture of the experimental system named Magnetic-Strung Nonlinear Energy Sink (MS-NES). This system contains mechanical components, such as masses, strings, and springs, along with electromechanical components and magnets. Thus the next few sections will sequentially introduce each of the interacting components into the governing equations of this NES system. The current section starts by deriving the governing equations for the mechanical components of the system while noting a primary complication; i.e. the need to precisely obtain a zero linear stiffness term in the NES. Later sections describe the electromechanical coupling and the zeroing of the aggregate linear stiffness through the use of permanent magnets.

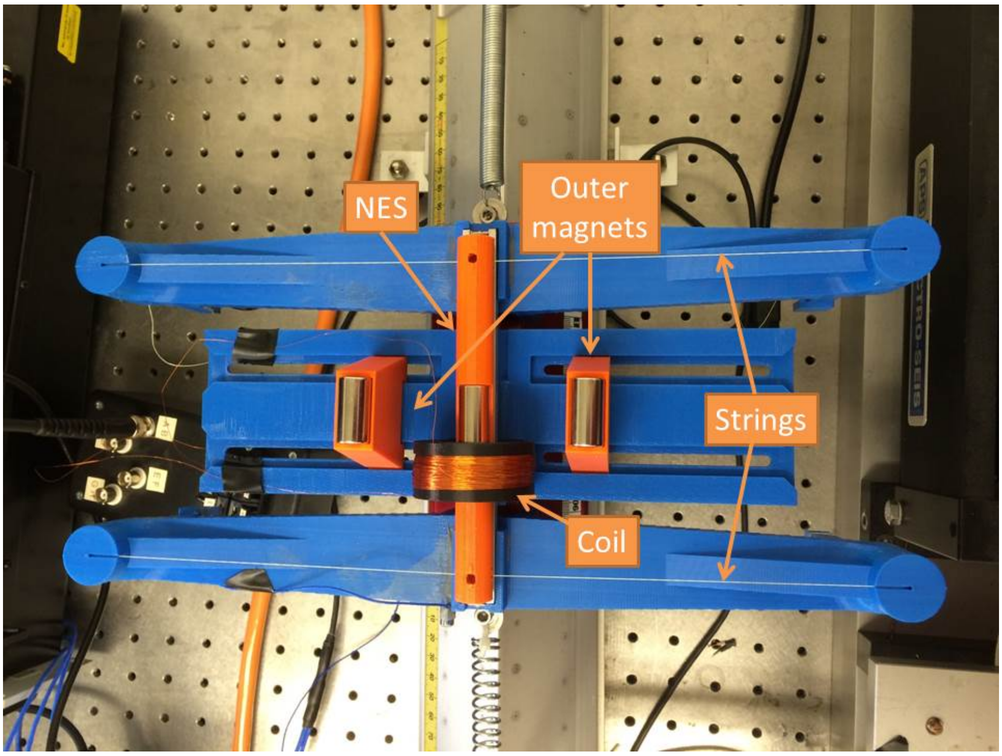

Figure 1: Top view of the system that was designed for experimental testing. This system contains mechanical components, an electric circuit, a coil, and additional magnets.

Figure 2 shows a schematic of the important mechanical components for the NES system. The primary system is presumed to be a linear oscillator (LO) that contains a mass M, spring

K and damper C. Base excitation, in the form of a harmonic displacement of X_e, is used to drive the system. The NES is composed of a small mass m that is coupled to the primary system through two elastic strings that are shown by the line segments $\overline{AB}$ and $\overline{BD}$. The strings act as elastic elements and provide the coupling force between the LO and the NES. The force acting on the mass m as a function of the displacement y can be approximated by the expression

$$F_{strings} = \frac{T_0}{L}y + \left(\frac{EA}{2L^3} - \frac{T_0}{2L^3}\right)y^3 + \mathcal{O}(y^5) \tag{1}$$

where T_0 is the pretension in the strings, E is the elastic modulus, and A is the cross sectional area of the strings. Thus, the restoring force caused by string deflection contains a term linearly proportional to the displacement, a term proportional to the cube of the displacement, and higher order terms which have been neglected. From Eq (1), the linear stiffness is $k_1 = \frac{T_0}{L}$ and cubic stiffness $k_3 = \left(\frac{EA}{2L^3} - \frac{T_0}{2L^3}\right)$. Both terms are a function of the string pretension T_0, a parameter that could be altered in the experiments. It is worth noting that the only way the linear stiffness component can be set to zero is to have absolutely no string tension. Unfortunately, this is difficult to achieve experimentally; though the approach used to attempt this effect is further discussed in the upcoming sections.

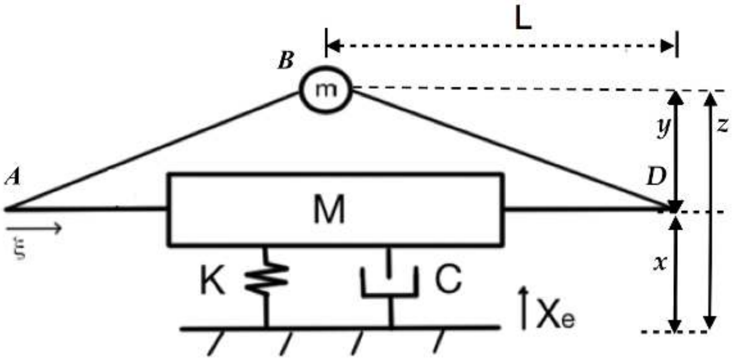

Figure 2: Schematic of the Strung-NES. View from the top. $\overline{AB}$ and $\overline{BD}$ are the strings which act as elastic elements.

Defining the absolute displacement of the NES mass as $z = x+y$, the equations of motion of the system can be written as

$$\begin{gathered} M\ddot{x} + c\dot{x} + kx + k_1(x-z) + k_3(x-z)^3 + c_1(\dot{x}-\dot{z}) = kX_e + c\dot{X}_e \\ m\ddot{z} + c_1(\dot{z}-\dot{x}) + k_1(z-x) + k_3(z-x)^3 = 0 \end{gathered} \tag{2}$$

where an overdot indicates a derivative with respect to time, where M, k and c are respectively the mass, the stiffness, and the damping of the primary system, where m is the mass of the NES, and where c_1, k_1 and k_3 are respectively the damping, the stiffness linear term and the stiffness cubic term related to the relative motion between the NES and the primary system.

An important feature of an NES is that it should have no linear natural frequency. This feature, albeit difficult to achieve experimentally, is precisely the characteristic that allows the NES to tune itself to the primary system and to be an effective vibration absorber over a broad range of frequencies. Note that achieving an aggregate linear stiffness of zero or the complete absence of a linear stiffness component would both achieve the goal of a zero linear natural frequency. As mentioned previously, the linear stiffness for the mechanical system described thus far is only zero if there is no string pretension. During experimentation, it was difficult to have absolutely no tension in the string and simultaneously avoid free-play, a small region with no restoring force as the mass is displaced. Therefore a counter-balance in the form of magnet-magnet interactions will be introduced into the mathematical model in Section 2.2.

2.1. Electromechanical coupling

This section derives the equations for the electromechanical coupling in the system. The important components are shown in both the picture of Fig. 1 and in the schematics of Figs. 3 and 4. In particular, Fig. 1 shows the NES mass is a magnet that oscillates through the center of a coil. The electromotive force can be described with Faraday's Law

$$\varepsilon = -\frac{\mathrm{d}\Phi_B}{\mathrm{d}t} \tag{3}$$

where ε is the electromotive force and Φ_B is the magnetic flux. The conceptual idea of combining the NES and harvester is shown in Fig. 3. The oscillations or vibrational energy of the primary system flows to the NES and is finally converted into electric energy through the harvester.

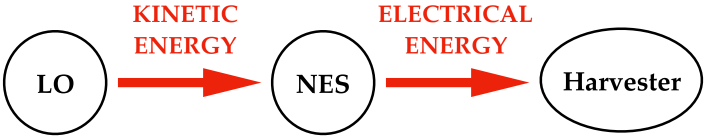

Figure 3: Schematic of the energy flow from the linear oscillator to the harvester.

As derived in reference [27], the oscillating magnet and closed circuit of the coil introduce coupling terms into the mechanical system and an additional equation for the electrical circuit. Assuming the simple electrical circuit shown in Fig. 4, which only contains a single electrical load, the governing equations become:

$$\begin{gathered} M\ddot{x} + c\dot{x} + kx + k_1(x-z) + k_3(x-z)^3 + c_1(\dot{x}-\dot{z}) = kX_e + c\dot{X}_e \\ m\ddot{z} + c_1(\dot{z}-\dot{x}) + k_1(z-x) + k_3(z-x)^3 - \gamma I = 0 \\ L\dot{I} + (R_L+R_i)I + \gamma(\dot{z}-\dot{x}) = 0 \end{gathered} \tag{4}$$

where I is the current in the electrical circuit, L is the coil's inductance, R_i is the coil's internal resistance, R_L is the resistive load within the electrical circuit, and γ is an electromechanical coupling term. It should be noted that in the electrical circuit of Fig. 4 no electromotive force has been represented since the electrical current is generated by the relative motion between the magnet and the coil. In the system Eq. (4) the electromotive force appears in the third equation as $\gamma(\dot{z} - \dot{x})$.

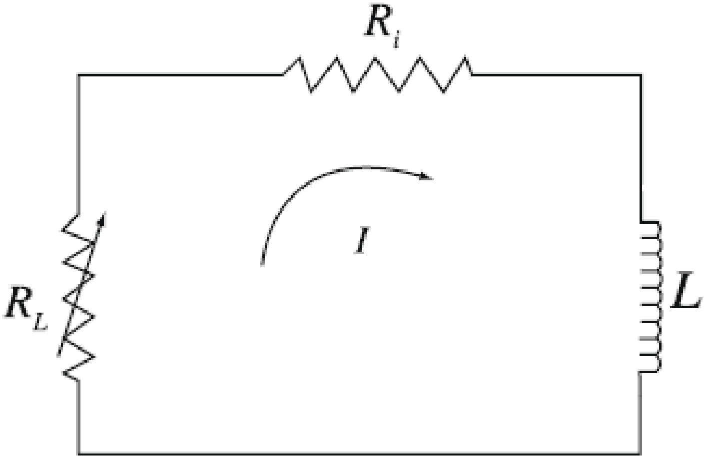

Figure 4: Schematic of the coupled electrical circuit: R_i and L are the resistance and the inductance of the coil, R_L is the resistive load the current I is delivered to.

2.2. Magnetic counterbalance

A primary challenge in experimentally realizing a NES system is the difficulty associated with creating a mechanical system with no linear stiffness. Instead of attempting to create this effect with a single mechanical component, this work explored the interaction between permanent magnets to create a counterbalance effect. More specifically, magnetic repulsion forces were used to cancel out the inherent linear stiffness in the original mechanical system. To elaborate, Fig. 5 shows a schematic of the NES primary mass which is constrained to translate in the y direction. The addition of two neighboring magnets, located a distance of R_o away, provided a repulsive force to counter the linear component of the mechanical restoring force. While several aspects of the derivation parallel the approach presented in reference [35], the authors have chosen to include this derivation for completeness and to ensure the subtle differences are not overlooked. The potential energy and force expressions were derived from a dipole model (Ref.[36, 37]). The magnetic flux density, or **B**-field, at the location $\mathbf{r}_p$, due to a magnet located at $\mathbf{r}_s$, is given by

$$\mathbf{B} = -\frac{\mu_0}{4\pi}\nabla\frac{\mathbf{m}_s \cdot \mathbf{r}_{p/s}}{|\mathbf{r}_{p/s}|^3} \tag{5}$$

where ∇ indicates the vector gradient, where $\mu_0 = 4\pi \times 10^{-7}$ H/m is the permeability of free space, and where $\mathbf{r}_{p/s}$ is the relative position vector to the point of interest $\mathbf{r}_p$ from a

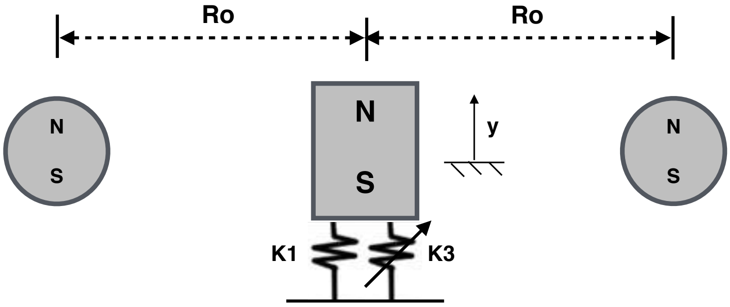

Figure 5: Schematic of the NES mass (center magnet) shown with two outer magnets that could slide along the tracks shown in Fig. 1 to alter the distance R_o between the NES mass (or magnet) and the outer magnets.

source magnet located at $\mathbf{r}_s$. The term $\mathbf{m}_s = \mathbf{M}_s v_s$ is the magnetic moment of the magnet located at $\mathbf{r}_s$, and $\mathbf{M}_s$ and v_s are the magnetization and volume, respectively, of the source magnet. The potential energy of the magnet at $\mathbf{r}_p$ in the field generated by the magnet at $\mathbf{r}_s$ is

$$\mathcal{U} = -\mathbf{m}_p \cdot \mathbf{B} \tag{6}$$

By applying Eqs. (5) and (6) to the schematic of Fig. 5, the following expression was obtained for the potential energy of the magnet interactions

$$\mathcal{U} = -\frac{\mu_0 M_c v_c}{2\pi} \frac{M_o v_o N}{2} \left(\frac{y^2}{(y^2 + R_o^2)^{5/2}} - \frac{1}{(y^2 + R_o^2)^{3/2}} \right) \tag{7}$$

where M_c and v_c are the magnetization and the volume of the central magnet, M_o and v_o are the magnetization and the volume of the outer magnets, N is the number of outer magnets, R_o is the distance between the outer magnets and the central magnet (i.e. the NES mass), as displayed in Fig. 5. In this study three magnets are used, one central and two outer ($N = 2$), all having the same properties and dimensions: $M_c = M_o = 1.05 \times 10^6$ A/m, $v_c = v_o = 2.24$ mm^3.

The interaction force between the two magnets can then be obtained from the gradient of equation (6). Thus the magnetic restoring force F_m is the derivative of (7) with respect of y

$$F_m = -\frac{\mu_0 M_c v_c M_o v_o}{2\pi} \left(\frac{5y}{(y^2 + R_o^2)^{5/2}} - \frac{5y^3}{(y^2 + R_o^2)^{7/2}} \right) \tag{8}$$

Inserting F_m into Eq. (4) gives the final form for the governing equations of motion

$$\begin{gathered} M\ddot{x} + c\dot{x} + kx + k_1(x - z) + k_3(x - z)^3 + c_1(\dot{x} - \dot{z}) = kX_e + c\dot{X}_e \\ m\ddot{z} + c_1(\dot{z} - \dot{x}) + k_1(z - x) + k_3(z - x)^3 + F_m - \gamma I = 0 \\ L\dot{I} + (R_L + R_i)I + \gamma(\dot{z} - \dot{x}) = 0 \end{gathered} \tag{9}$$

where the magnetic force $F_m = F_m(z - x)$ has been inserted into the previously derived equations.

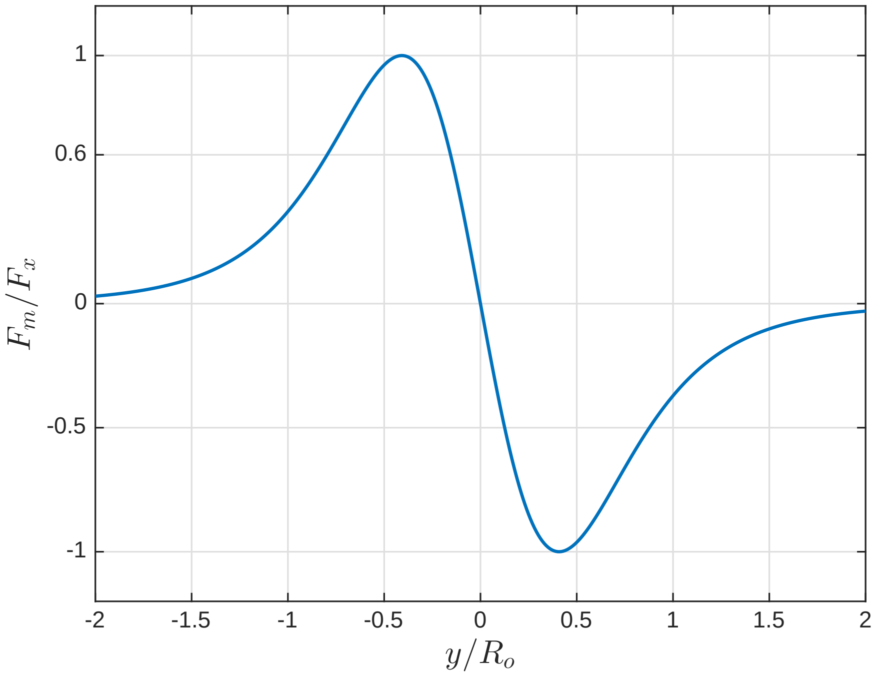

Figure 6: Normalized magnetic force versus normalized displacement curve generated from Eq. (8). Vertical axis is normalized by F_x or the maximum F_m value generated over the range $-2 \leq \dfrac{y}{R_o} \leq 2$.

A normalized force displacement curve, which uses the expression for F_m and its maximum value F_x, is shown in Fig. 6. As seen in the plot, the magnet-magnet interaction force is highly nonlinear over the normalized range of $-2 \leq \dfrac{y}{R_o} \leq 2$. For experiment design purposes, Eq. (8) can also be used to determine the magnet spacing $R_o = R_c$ that creates a counterbalance effect. This is where the linear component of the magnetic force exactly cancels the linear component of the mechanical restoring force. An expression for the counterbalance spacing R_c can be obtained by evaluating the derivative $\dfrac{\mathrm{d}F}{\mathrm{d}y}$ at $y = 0$ and setting it equal to k_1. Solving for R_o and then noting that $R_o = R_c$ at this position, gives the following expression:

$$R_c = \sqrt[5]{\frac{5\mu_0 M_c v_c M_o v_o}{2\pi k_1}} = \sqrt[5]{\frac{5\mu_0 M_c v_c M_o v_o L}{2\pi T_0}} \tag{10}$$

this expression has been given in terms of both k_1 and the string tension T_0 by using the relation $k_1 = T_0/L$, where L represents the initial length of the strings as illustrated in Fig. 2.

Figure 7 shows a normalized force versus displacement curve when the counterbalance spacing R_c is used for the magnet spacing. This figure separately shows the mechanical

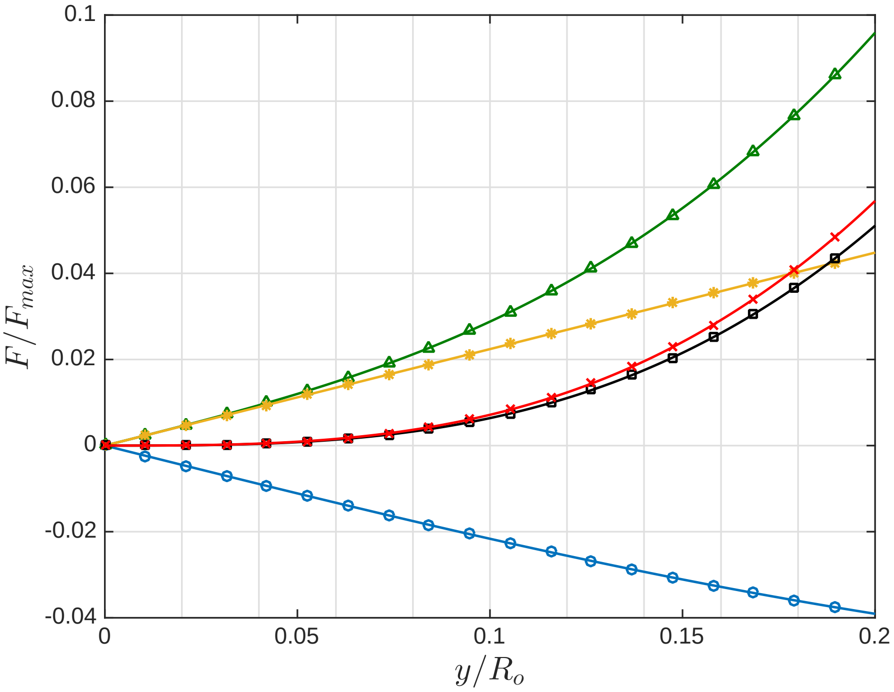

Figure 7: All the forces involved in the balancing: the total elastic force (green curve - triangles) and its linear (yellow - stars) and cubic (black - squares) components, the magnetic force (blue - circles) and the resulting force (red - crosses). The magnetic force cancels out the linear elastic component and as a consequence the total resulting force is essentially cubic.

and magnetic restoring forces along with the aggregate linear and nonlinear restoring force components, which were obtained by summing the mechanical and magnetic forces. As expected, the predicted counterbalance spacing acts to zero out the linear component of the aggregate or total restoring force, and only the nonlinear components of the restoring force remain.

2.2.1. Potential function counterbalance design

The previous section describes an approach for finding the magnet spacing R_c that enables the linear component of the magnetic repulsion force to cancel out the linear component of the restoring force from strings. This section describes an alternative approach for achieving the same effect. More specifically, the interaction between the elastic and the magnetic forces on the NES mass were described in terms of their potential energies.

As both the elastic string and magnetic forces are conservative, they can be obtained by taking the derivative with respect to the displacement y of the correspondent potential function $U = U(y)$.

Expressing the elastic potential energy as:

$$U_{el} = U_{k_1} + U_{k_3} = \frac{1}{2}k_1 y^2 + \frac{1}{4}k_3 y^4 \tag{11}$$

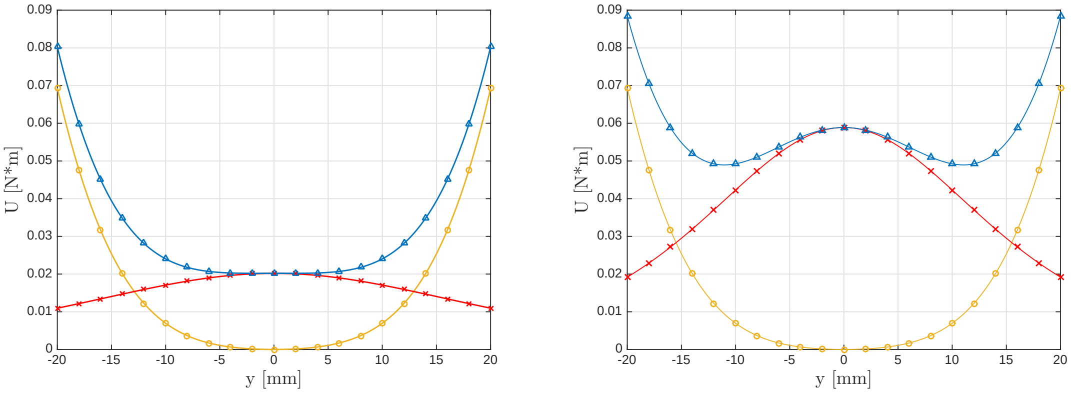

(a) (b)

Figure 8: Elastic potential energy (yellow - circles), magnetic potential energy (red - crosses) and their sum (blue - triangles) in the case of the cubic configuration (a) and the bistable configuration (b).

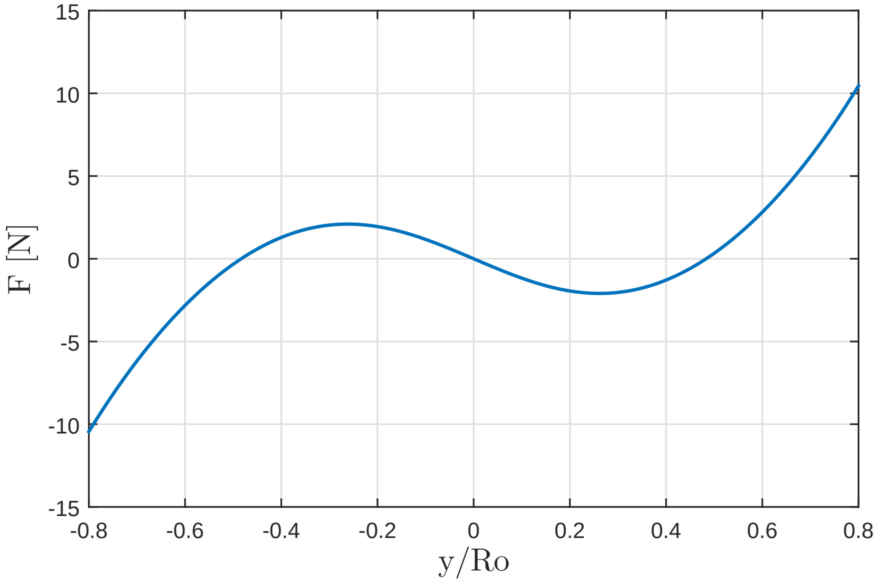

Figure 9: Nonlinear force between the primary system and the NES in the case of bistable configuration.

and the magnetic potential energy as expressed in Eq.(7), we can write the total potential energy $U_{tot}(y) = U_{el}(y) + U_m(y)$. By studying the evolution of U_{tot} as R_o varies, the stability of each configuration can be analyzed.

When there are no outer magnets ($R_o = \text{inf}$), the total potential energy is composed of only the elastic energy $U_{tot} = U_{el} = U_{k1} + U_{k2}$. The point $y = 0$ is the only equilibrium point, and it is stable as $\left.\frac{\mathrm{d}U}{\mathrm{d}y}\right|_{y=0} > 0$. If the outer magnets are placed at $R_o = \overline{R_o}$ so that the magnetic force cancels out the linear part of the elastic force, the equilibrium point $y = 0$ loses its stability and becomes neutrally stable as $\left.\frac{\mathrm{d}U}{\mathrm{d}y}\right|_{y=0} = 0$. This configuration, called *cubic*, is shown in Fig. 8a.

When the magnets are placed at a distance $R_o < \overline{R_o}$, the point $y = 0$ becomes unstable and two new stable points appear. The potential energies of this *bistable* configuration are illustrated in Fig. 8b. Fig. 9 shows the resultant nonlinear force between the primary system and the NES.

3. Electrical power delivered and viscous power dissipated

In order to estimate the efficacy of the Magetic-Strung NES (MS-NES) as an absorber and as a harvester, we define the average electrical power delivered and the average viscous power dissipated:

$$\overline{P}_{el}(t_0) = \frac{1}{t_0}\int_0^{t_0} P_{el}(t) \quad \overline{P}_{vis}(t_0) = \frac{1}{t_0}\int_0^{t_0} P_{vis}(t) \tag{12}$$

Where $P_{el}(t) = R_L I^2(t)$ is the the electrical power delivered to the resistive load R_L and $P_{vis}(t) = C_1(\dot{z} - \dot{x})^2$ is the power dissipated by the viscous damping C_1 between the primary system and the NES.

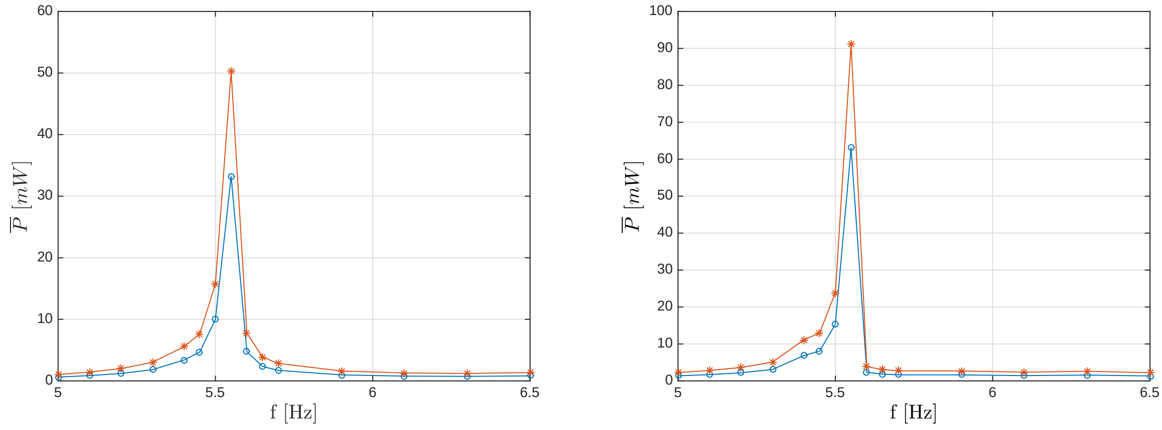

(a) (b)

Figure 10: Numerical Frequency-Power Function for the no-magnet (a) and the cubic (b) configuration for an external forcing $\ddot{x}_e = 0.6$ m/s^2. The values used in these simulations are those of the experimental apparatus presented in the next section (Tab1, Tab.2). It can be seen that the viscous power dissipated (red stars) and the electrical power delivered (blue circles) are significantly higher in the case of cubic MS-NES.

These new quantities have a particular interest as they can be used to describe the efficacy and performance of the MS-NES when strongly nonlinear phenomena arise in the response. For example, when in a forced regime the response is not steady but periodical or even chaotic, these measurements provide an accurate estimation of the energy dissipated and converted as they reach a steady value as $t \to \infty$:

$$\overline{P}_{el_\infty} = \overline{P}_{el}(t \rightarrow \infty) \quad \overline{P}_{vis_\infty} = \overline{P}_{vis}(t \rightarrow \infty) \tag{13}$$

In practice, a steady value is reached even after a few cycles. It is possible to calculate a steady value $\overline{P}_{el_\infty}$ and $\overline{P}_{vis_\infty}$ at each frequency and amplitude of external excitation .

We present in Fig. 10 the Frequency-Power plots for the no-magnets configuration and the cubic configuration of the MS-NES. The peak of energy dissipated and delivered is significantly higher in the case of cubic configuration: 60 mW and 40 mW respectively for the no-magnets, whereas 95 mW and 65 mW for the cubic.

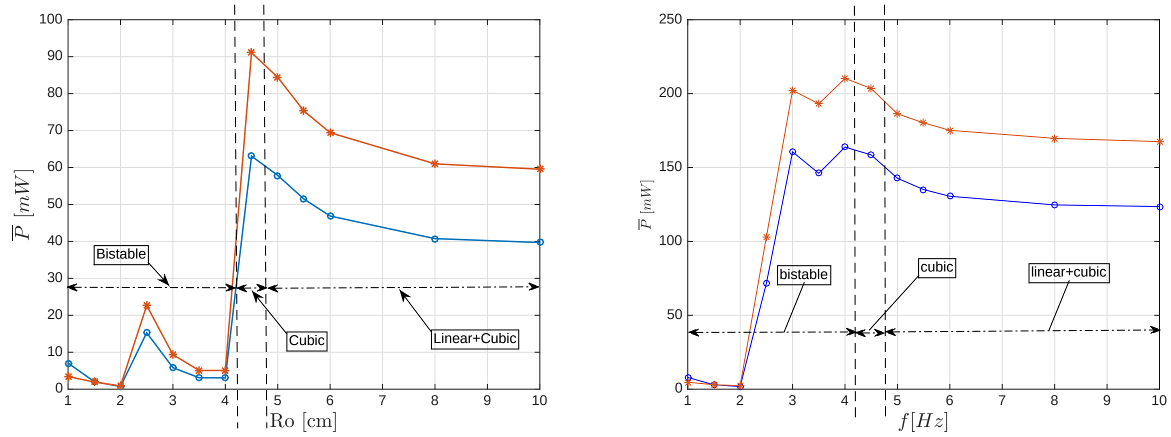

(a) (b)

Figure 11: Average Power Delivered (blue circles) and Average Power Dissipated (red stars) as a function of the outer magnets distance Ro. External forcing: $\ddot{x}_e = 0.6$ m/s^2 - $f = 5.57$ Hz (a); $\ddot{x}_e = 1.8$ m/s^2 - $f = 5.57$ Hz (b).

Since we have identified the peak frequency at $f = 5.57$ Hz, it is possible to evaluate the powers (dissipated and delivered) by keeping constant the frequency and varying the magnets distance. Fig. 11 shows $\overline{P}_{el_\infty}$ and $\overline{P}_{vis_\infty}$ for a level of external excitation of $\ddot{x}_e = 0.6$ m/s^2. It can be seen that the performances get better as the distance Ro deceases down to a distance $Ro \approx 4.5$ cm. Eq.(10) indicates that this distance corresponds to a cubic configuration ($R_c = 4.4$ cm). After that, the powers drastically drop down. This behavior can be explained by the fact that, since the configuration becomes bistable, the NES mass becomes stuck in a potential well and does not have enough energy to escape.

If the level of external excitation is higher ($\ddot{x}_e = 1.8$ m/s^2), the performances continues improving even for a smaller distance Ro. This scenario is displayed in Fig. 11.

4. Description of the prototype

In Fig. 12 the prototype is shown. All the blue and the orange pieces have been 3D printed at Duke University. The lower part is a cart sliding on an airtrack that minimizes the friction of the primary system. The two sides attached to two sprigs, with one connecting to the ground and the other to the shaker. The NES is a magnet which is placed into a hollow tube and onto a nonmagnetic low-friction slider upon the primary mass. The NES is connected to the primary mass by means of two strings which work transversely when the NES oscillates. On the sides of the NES the two outer magnets can be noticed; it is important to highlight that their distance to the NES is adjustable in order to reach the suitable force shape. Finally, the coil through which the NES mass oscillates is placed on the primary mass.

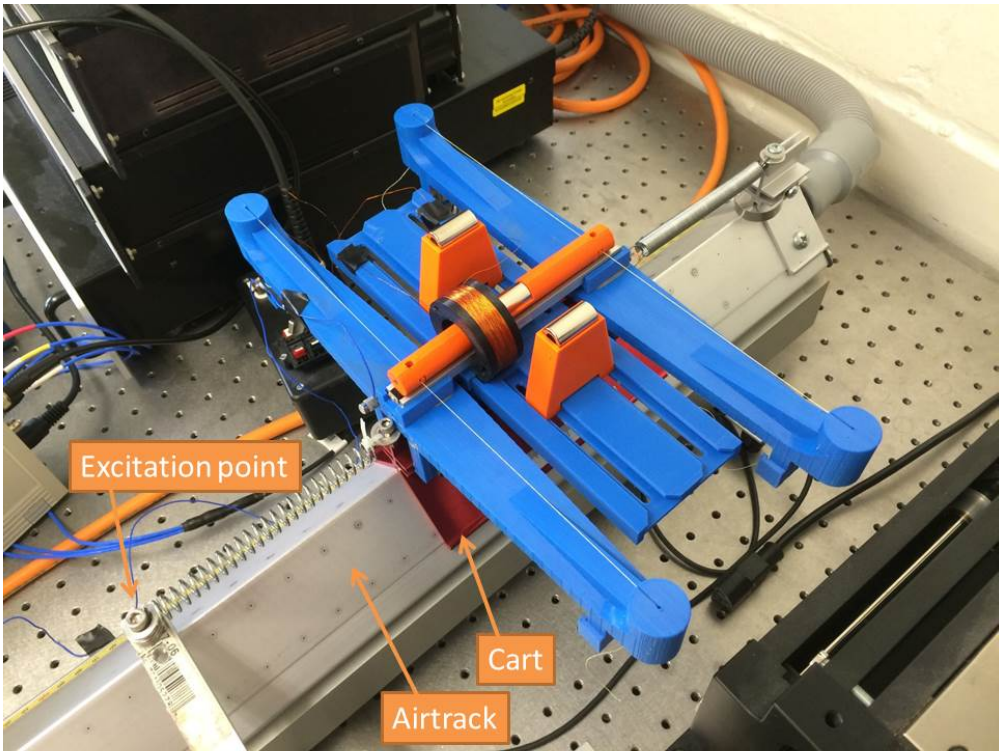

Figure 12: The prototype of the Magnetic-Strung NES.

4.1. *Identification of the coupled electro-mechanical system*

The modal parameters of the primary system were obtained from free oscillation measurements, and are listed in Tab.1 along with the mass ratio between the NES and primary system.

$f_n[Hz]$	$K[N/m]$	ξ	$\epsilon = m/M$
5.6	1223	0.036	0.04

Table 1: Modal parameters of primary system.

The electrical parameters have been experimentally measured and are listed in Tab.2, where L is the coil's inductance, R_i is the coil's internal resistance, R_L is the resistive load and γ is a transducer constant that couples the mechanical and the eletrical system.

$L[H]$	$R_L[\Omega]$	$R_i[\Omega]$	$\gamma[Vs/m]$
$100 \times 10^{-}3$	100	3500	-3.2572

Table 2: Electrical parameters.

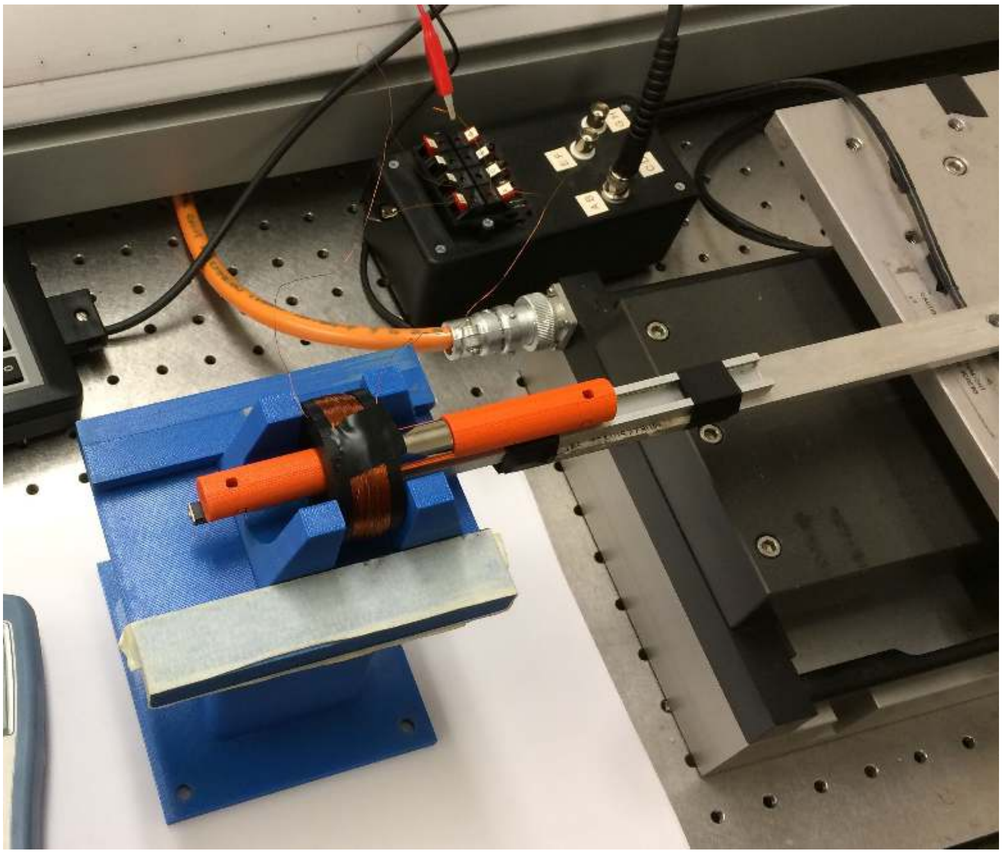

Figure 13: Experimental apparatus used to evaluate the transducer constant γ coupling the mechanical and the electrical system.

An extensive study on the nonlinear electromagnetic coupling between a coil and an oscillating magnet is presented in [38].

In this work, the term γ was experimentally evaluated as follows: taking the electrical equation of Eq. (4) governing the circuit shown in Fig. 4 it can be seen that, for a steady condition, if the relative velocity $\dot{y} = \dot{z} - \dot{x}$ is known and by measuring the current I, the only unknown is the constant γ, which therefore can be evaluated.

$$L\dot{I} + (R_L + R_i)I + \gamma(\dot{z} - \dot{x}) = 0 \qquad (14)$$

The experimental apparatus in shown in Fig. 13. The magnet was placed on the shaker, and it oscillated through the coil which was at rest ($\dot{x} = 0$), i.e. $\dot{y} = \dot{z}$. Since the harmonic motion of the magnet was known, the constant γ was finally estimated as $\gamma = -3.2572\, Vs/m$

by measuring the voltage across the coil.

It is important to notice that the values of the electrical parameters L, R_i, R_L and γ used to obtain the results that follow, were not optimized in order to maximize the energy harvested. While the objective of this work is the observation and the experimental validation of the theoretical concept, an optimization process will be carried out in future research. This process will need to simultaneously take into account both the vibration reduction and the energy harvesting aspects. These two aspects are actually related; by looking at Sys.(9), it can be seen that the electromechanical coupling adds some damping to the mechanical system. However, experimental measurements have shown that for the prototype studied in this work, the electrical damping was negligible compared to the mechanical one, so it can be considered that the electrical system has no effect on the mechanical one.

4.2. Experimental verification of the cubic stiffness

The efficacy of the outer magnets was subsequently tested experimentally. Static tests were performed in order to measure the elastic force provided by the strings and to obtain a force-displacement graph.

The NES magnet and the two outer magnets were identical and their magnetization and dimensions are listed in Tab. 3

$M[A/m]$	$d_o[mm]$	$d_i[mm]$	$l[mm]$
1.05×10^6	12.7	7.0	25.4

Table 3: Magnetization and dimensions of the NES and the outer magnets.

First the configuration with no outer magnets was tested. The force-displacement measurements are shown in Fig. 14 as blue dots. These points have been polynomial interpolated using a linear and a cubic term: $F = k_1 y + k_3 y^3$, which allows us to estimate the linear and the cubic stiffness displayed in Tab. 4).

$k_1[N/m]$	$k_3[N/m^3]$
112.25	1.38×10^6

Table 4: Linear and cubic stiffness for the configuration without outer magnets.

Knowing the linear stiffness k_1, the distance R_o was calculated using Eq.(15) in order to cancel out the linear term and to obtain an essentially cubic relation.

$$R_o = \sqrt[5]{\frac{5|C|}{k_1}} = 4\,\text{cm} \tag{15}$$

The measured points when the magnets were put at a distance $R_o = 4$ cm are shown in Fig. 14 as red dots. As for the the previous configuration, they have been polynomial

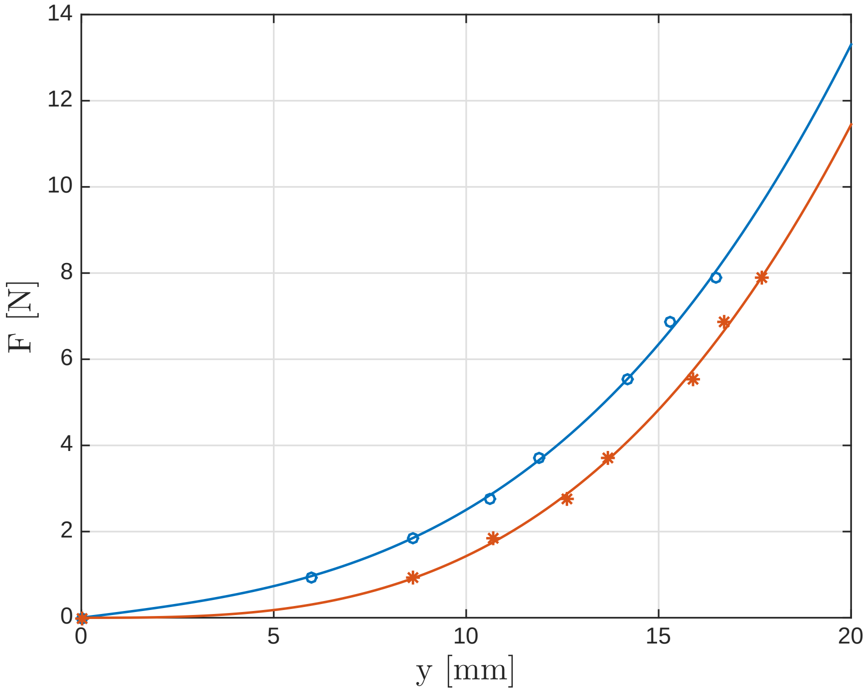

Figure 14: Experimental force-displacement relation without (blue-circles) and with (red-stars) outer magnets. The experimental points have been fitted by means of the polynomial expressions $F = k_1 y + k_3 y^3$.

interpolated using a linear and a cubic term: $F = k'_1 y + k'_3 y^3$. The coefficients obtained are shown in Tab.5..

$k'_1 [N/m]$	$k'_3 [N/m^3]$
0.42	1.43×10^6

Table 5: Linear and cubic stiffness for the configuration with outer magnets.

Therefore, as theoretically predicted, the presence of the outer magnets essentially allows for cancellation of the linear term of the elastic force and the ability to obtain a quasi-essential cubic relation, crucial aspect to fully take advantage of the characteristics of a nonlinear vibration absorber.

5. Experimental results

The system was harmonically forced by the base motion at several amplitudes and frequencies. The aim was to observe the types of response the system could exhibit and to study its performance in terms of energy absorption and harvesting. The primary mass and the moving base were equipped with accelerometers. The NES motion was monitored by using the signal issued by the coil, i.e. the voltage across the coil. This voltage can be considered proportional to the magnet velocity.

The results illustrated are issued from the same case of external excitation (0.6 m/s^2 at 6.2 Hz) and for three different configurations of the MS-NES. In the first configuration the outer magnets are not used so the relation between the absorber and the primary system is not completely nonlinear but presents the linear term. In the second configuration, called *cubic*, the outer magnets are placed at a distance which allows the magnetic force to perfectly cancel out the linear term and the resulting force to be purely cubic. The third configuration is the so-called Bi-stable and the resulting force has a shape as illustrated in the previous section.

For each configuration, a kinematic study is firstly conducted. The phase diagram as well as the Poincaré sections of the system's responses are obtained in order to evaluate their periodicity. Subsequently, the capability of the MS-NES as a vibration absorber and as an energy harvester is analyzed. According to theory, this specific excitation frequency is where the Strongly Modulated Responses are expected to appear. In fact, results have shown that depending on the distance of the magnets (i.e. on the shape of the force between LO and MS-NES), the system can exhibit different types of response going from periodic to chaotic.

5.1. No outer magnets

In this configuration, the outer magnets are not used, meaning that in Eq. (4) the magnetic force F_m is zero. The expression for the restoring elastic force between the MS-NES and the primary system is: $F = k_1(z-x) + k_3(z-x)^3$.

Concerning the kinematic study, in Fig. 15a the displacement and the velocity of the NES mass are shown. The envelope has been highlighted. Fig. 15b shows the phase diagram $y - \dot{y}$ of the response. The red dots on the phase diagram represent the Poincaré map of the envelope.

In Fig. 15 the solution reached by the system can be observed to be steady and the response amplitude constant. The trajectories in the phase diagrams are ellipses and all the points in the Poincaré map are gathered in the same area; we can conclude that the global behavior is totally deterministic. It should be noticed that the Poincaré map of the envelope is represented, as a consequence the trajectories of the phase space diagram do not go through the points of the map.

After studying the kinematics of this configuration we go further by analyzing the energetic aspects of the system. We are interested in studying the energy flow from the primary system to the NES, and in evaluating the portion of energy which is dissipated by viscous friction and the amount which is converted into electrical energy.

In Fig. 16 (a), the instantaneous kinetic energy during the recorded time interval of the primary system and of the NES is shown. The lower part shows the instantaneous electrical energy delivered to the resistive load $P_{el} = I^2 R_L$. As concluded after the kinematic analysis, the system exhibits a steady solution: an equilibrium is reached between the vibrating energy held in the primary system and the portion of energy transferred to the NES.

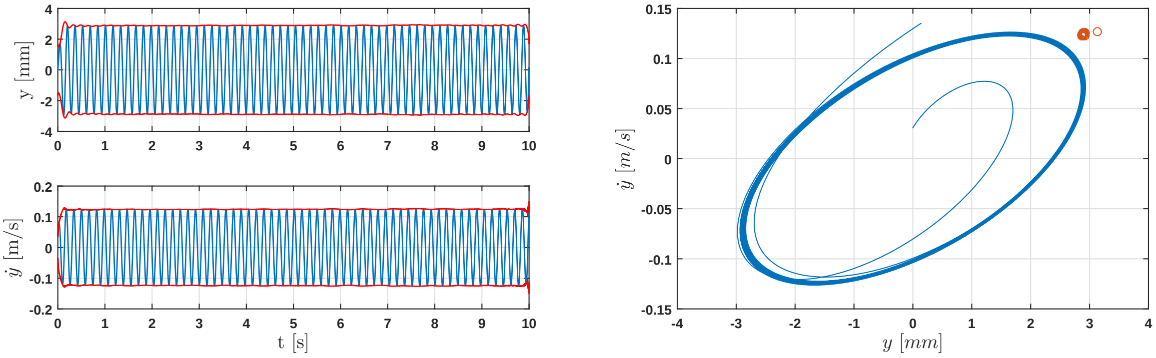

(a)

(b)

Figure 15: NES displacement y and velocity $\dot{y}$ (a) in the configuration without outer magnets and its phase diagram (b). The envelope of the response is highlighted and its Poincaré Map represented by red dots in the $y-\dot{y}$ space. The global system behavior is totally deterministic and the regime steady.

We can have a better understanding of how the energy is distributed in the system by calculating the ratio between the energy located into the NES and the total energy present in the system. The energy ratio is a good indicator of the vibration absorption performance of the system.

$$\frac{E_{NES}}{E_{TOT}} = \frac{T_{NES}+U_{NES}}{T_{LO}+U_{LO}+T_{NES}+U_{NES}} \tag{16}$$

The energy ratio throughout the time is illustrated in Fig. 17: about half the total energy of the system is located into the NES.

The energy transferred to the NES is then partially dissipated by the viscous damping and partially converted into electrical energy.

In Fig. 18 the average electrical power delivered and the average viscous power dissipated as defined by Eq.(12) are shown. Because of the steady nature of the response, the two quantities quickly reach their asymptotic values.

5.2. Cubic

Here the results obtained from the tests performed on the *cubic* configuration are illustrated. As explained in Sec. 2.2, it is possible to calculate the distance of the outer magnets R_o in order to obtain a purely cubic relation between the primary system and the NES. For a linear elastic term $k_1 = 69.4$ N/m, the distance was estimated to be $R_o = 4$ cm.

The external forcing amplitude and frequency are equal to the values found in the previous section: 0.6 m/s^2 at 6.2 Hz.

We first focus on the kinematic of the response and subsequently discuss the energetic aspects. In Fig. 19a the displacement and the velocity of the NES mass are shown and their envelope has been highlighted in red. In Fig. 19b the phase diagram $y-\dot{y}$ is shown as well as the Poincaré map of the envelope (red dots).

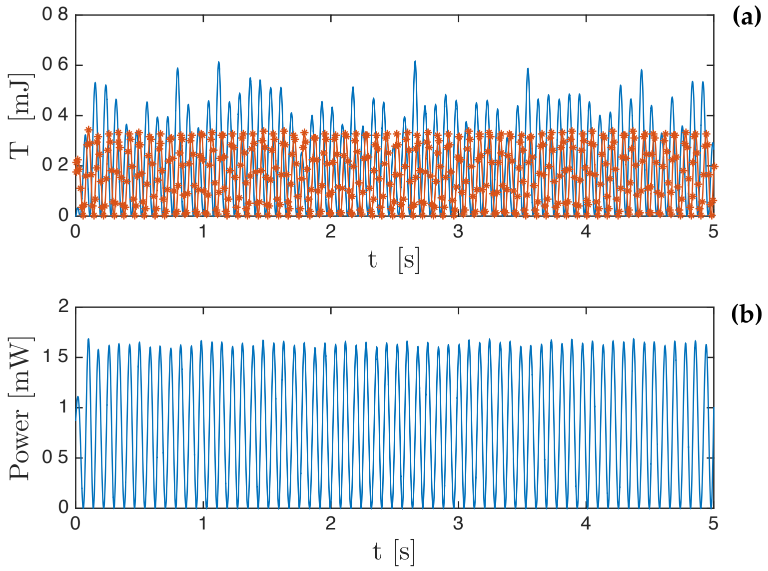

Figure 16: No magnets configuration: instantaneous kinetic energy of the primary system ((a) - blue) and of the NES ((a) - red stars figure) and instantaneous electrical power delivered to the resistive load (b).

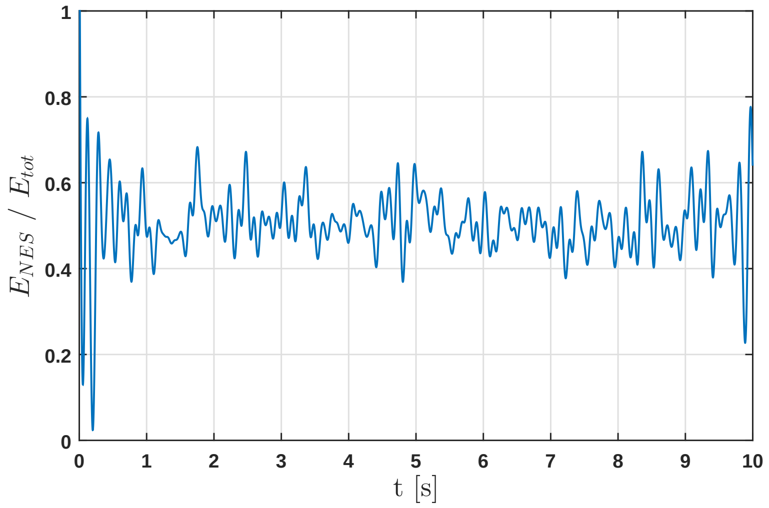

Figure 17: NES-LO Energy ratio defined as: $\frac{E_{NES}}{E_{TOT}} = \frac{T_{NES}+U_{NES}}{T_{LO}+U_{LO}+T_{NES}+U_{NES}}$ in the configuration without outer magnets.

We can immediately see that the response of the system has become modulated: it is no longer steady but periodic. This kind of response is known in literature as Strongly Modulated Response (SMR) and is typically observed among nonlinear absorbers [3].

The phase diagram and the Poincaré map allow us to attest that although it appears to have a complex pattern the response is not chaotic. This can be deduced from the NES response in Fig. 19.

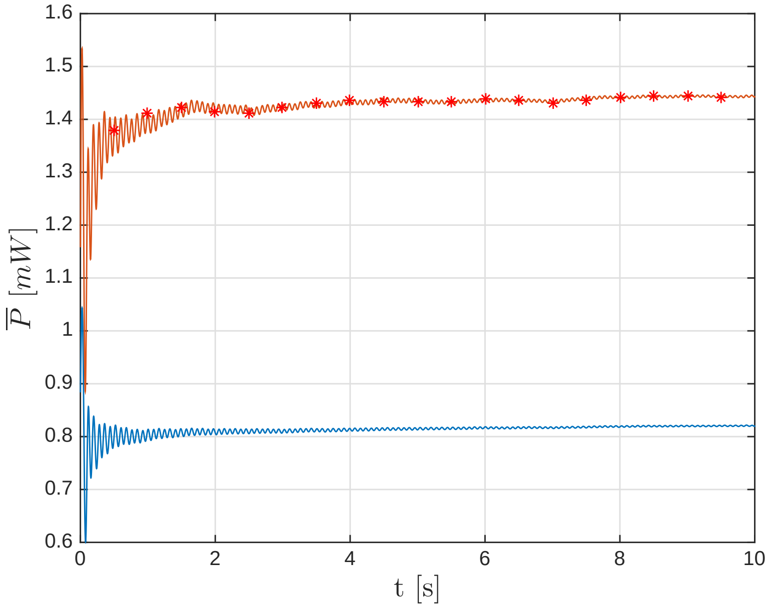

Figure 18: Average electrical power delivered (blue) and the average viscous power dissipated (red stars) in the configuration without outer magnets.

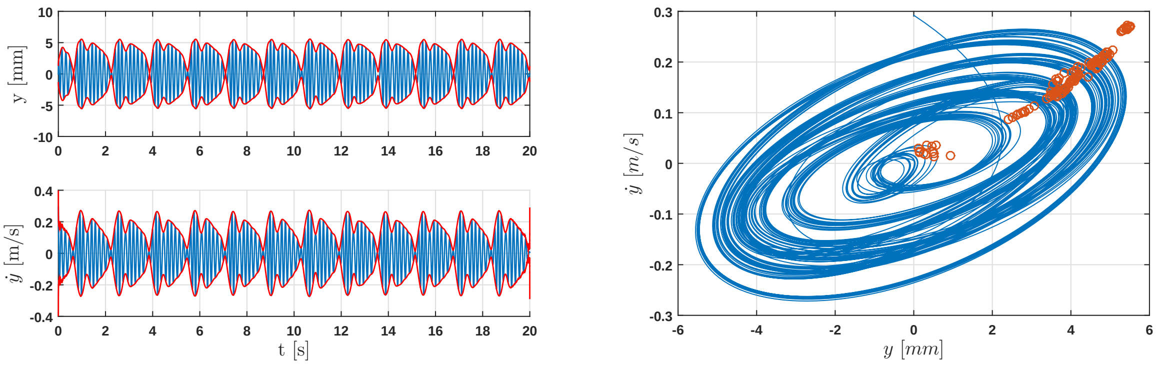

(a) (b)

Figure 19: NES displacement y and velocity $\dot{y}$ in the *cubic* configuration (a) and its phase diagram (b). The envelope of the response is highlighted in red and its Poincaré Map represented by red dots in the $y - \dot{y}$ space.

Fig. 20 shows the kinetic energy of the primary system and the NES (a) as well as the electrical power delivered to the resistance (b). It can be seen that the cycles the system completes are periodic and repetitive. In Fig. 21a a zoom of Fig. 20 illustrates the process of energy transfer from the primary system (LO) to the NES: the kinetic energy the primary system accumulates is transferred to the NES and subsequently partially dissipated through viscous damping and partially converted into electrical energy.

Fig. 21b describes the energy transfer mechanism by showing the energy ratio E_{NES}/E_{TOT}

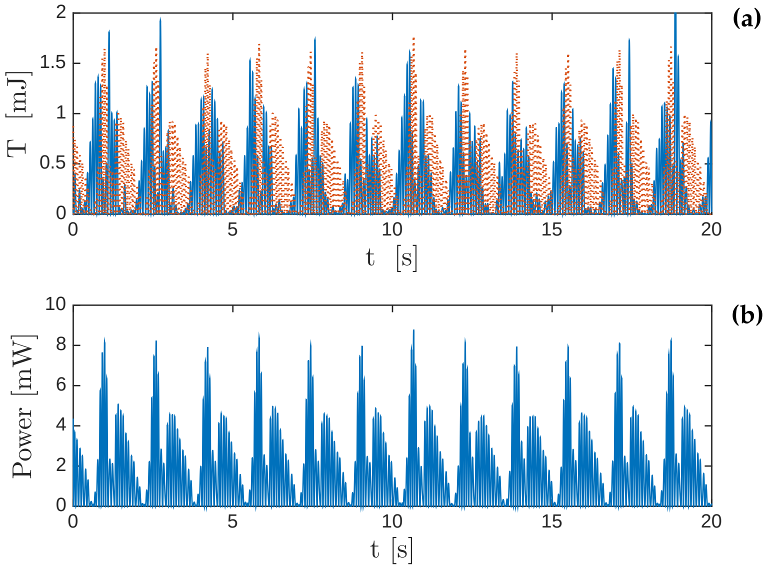

Figure 20: *Cubic* configuration: instantaneous kinetic energy of the primary system ((a) - blue solid line) and of the NES ((a) - red dotted line) and instantaneous electrical power delivered to the resistive load (b).

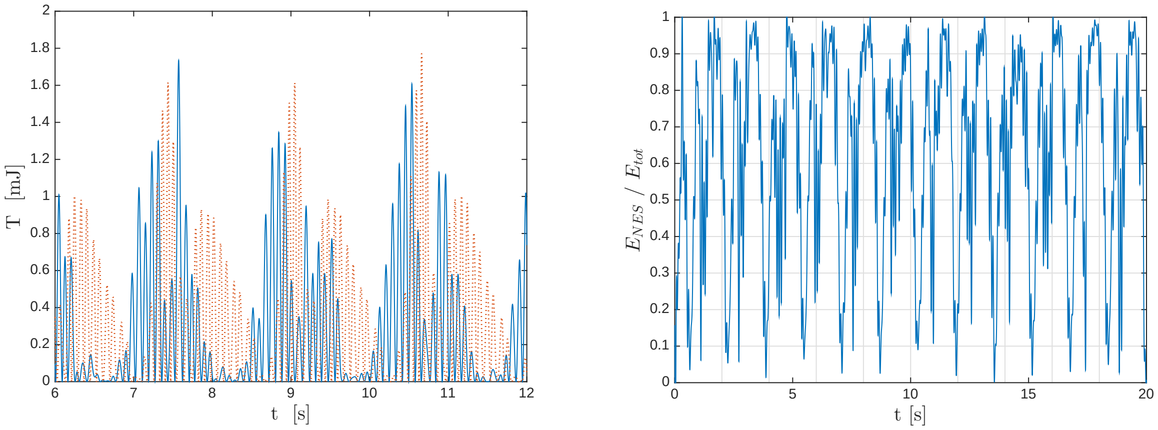

(a) (b)

Figure 21: Kinetic energy transfer (a) between the primary system (blue) and the NES (red) during the strongly modulated response of the *cubic* configuration and NES-LO energy ratio (b) defined as: $\frac{E_{NES}}{E_{TOT}} = \frac{T_{NES}+U_{NES}}{T_{LO}+U_{LO}+T_{NES}+U_{NES}}$.

as defined by Eq. (16): it can be seen that the total energy is cyclically entirely located into the NES.

Comparing the electrical power delivered in the two configurations without magnets (Fig. 16) and cubic (Fig. 20), we can see that in the latter configuration, the peaks of power reached are considerably higher than the value held constant by the first configuration.

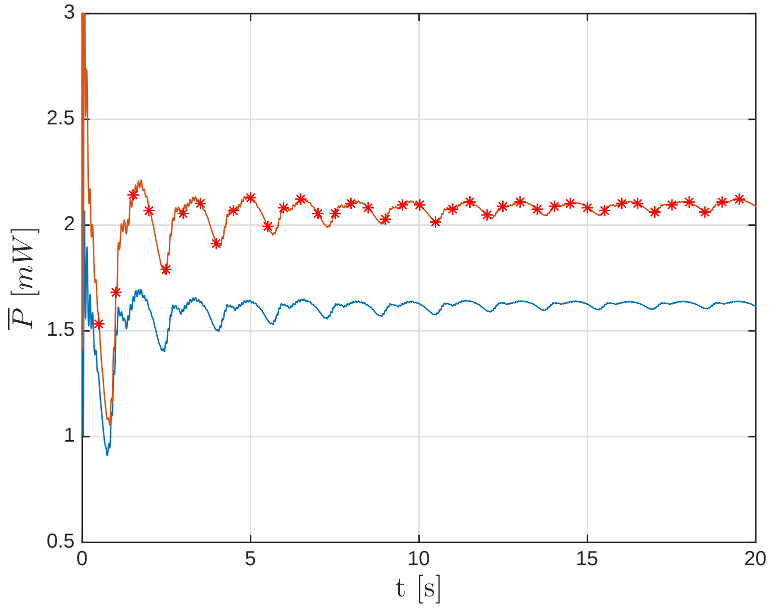

Figure 22: Average electrical power delivered (blue) and the average viscous power dissipated (red stars) in the *cubic* configuration.

The average power delivered and the average power dissipated as defined by Eq. (12) are displayed in Fig. 22: the asymptotic values $\overline{P}_{el_\infty}$ and $\overline{P}_{vis_\infty}$ are higher than those obtained by the previous configuration.

5.3. Bi-stable

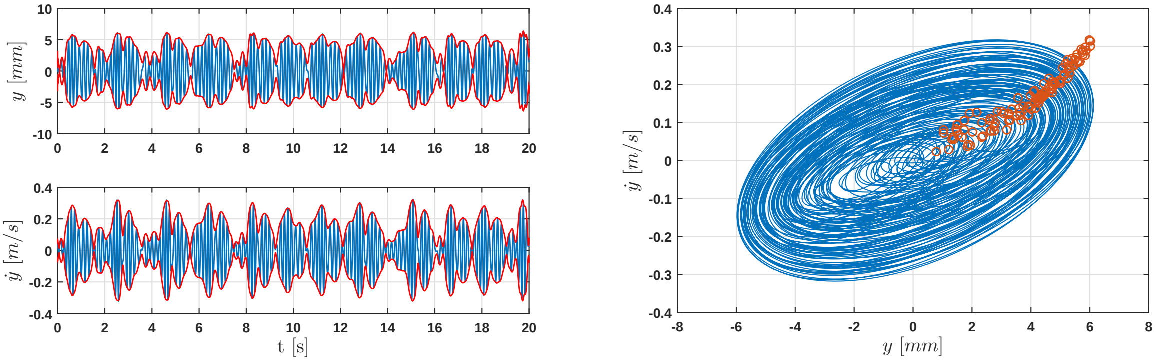

(a) (b)

Figure 23: NES displacement y and velocity $\dot{y}$ in the *bi-stable* configuration (left) and its phase diagram (right). The envelope of the response is highlighted in red and its Poincaré Map represented by red dots in the $y - \dot{y}$ space.

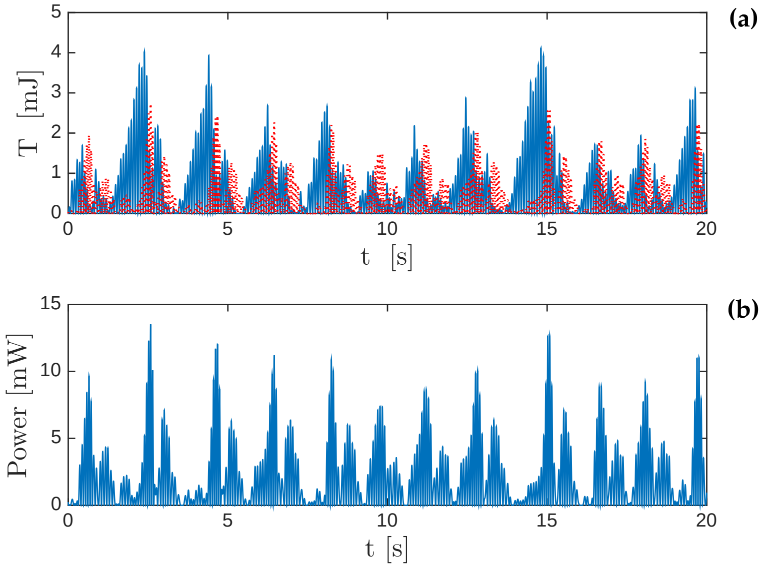

Figure 24: *Bi-stable* configuration: instantaneous kinetic energy of the primary system ((a) - blue solid) and of the NES ((a) - red dotted) and instantaneous electrical power delivered to the resistive load (b).

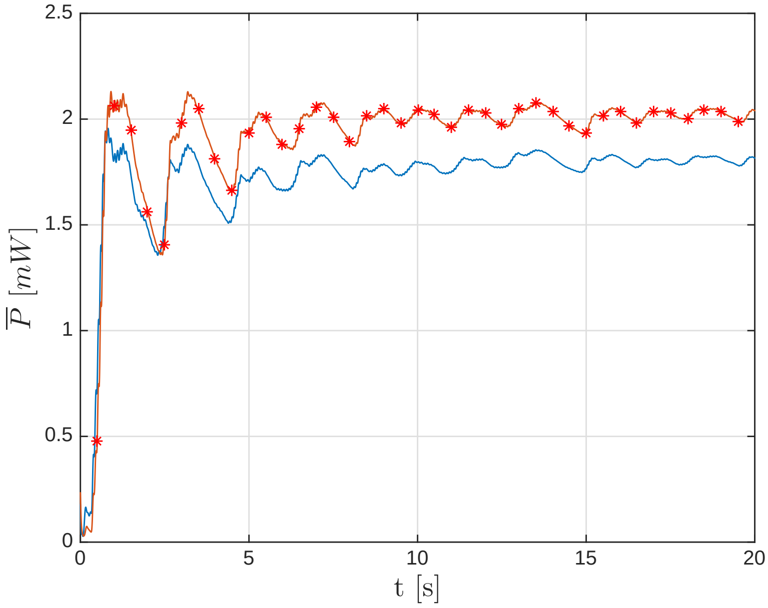

Figure 25: Average electrical power delivered (blue) and the average viscous power dissipated (red stars) in the *bi-stable* configuration.

The third configuration tested is the *bi-stable* configuration. As explained in Sec. 2.2.1, this configuration is obtained by placing the outer magnets at a distance R_o smaller than that canceling out the linear elastic term. The force-displacement relation has a shape as shown in Fig. 9 where three equilibria exist: one unstable ($y = 0$) and two stable ($y = \pm d$).

By examining Fig. 23 it can be seen that the response is still strongly modulated but this time the cycles appears to be more chaotic, as no specific periodicity can be identified.

The lack of periodicity in the system's response can also be observed by looking at the kinetic energy transfer and the electrical power delivered shown in Fig. 24. Each cycle seems to have its own shape. As a general observation, the peaks of kinetic energy reached in this configuration are higher than those attained in the cubic configuration.

The average power dissipated and the average power delivered are shown in Fig. 25. If compared to the cubic configuration, we can notice a slight improvement in the electrical power, whereas the viscous power is essentially the same as previously observed.

In essence, the bi-stable configuration generates a chaotic kinematic behavior of the NES which may potentially be favorable in terms of energy absorption and harvesting. Although the experimental results here presented do not show a significant improvement compared to those obtained with the cubic configuration, it may be worth carrying out a more extensive study on this configuration, which would include an optimization process.

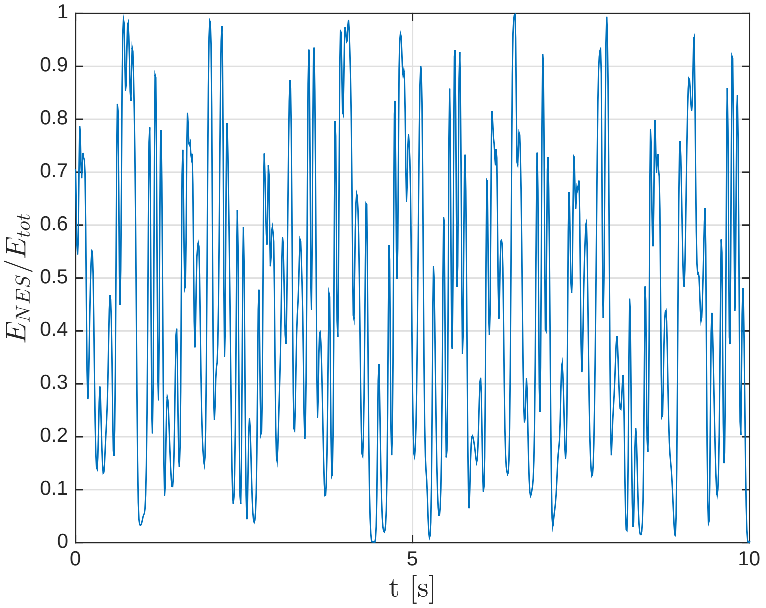

Figure 26: NES-LO Energy ratio defined as: $\frac{E_{NES}}{E_{TOT}} = \frac{T_{NES}+U_{NES}}{T_{LO}+U_{LO}+T_{NES}+U_{NES}}$ in the bistable configuration.

6. Bifurcation diagrams

The experimental observations show that, for an identical external forcing, the MS-NES may exhibit several types of response depending on the distance of the outer magnets R_o. More specifically, it was observed that the response goes from appearing completely steady and deterministic when the magnets are not used, to being non-deterministic in the case of the bistable configuration.

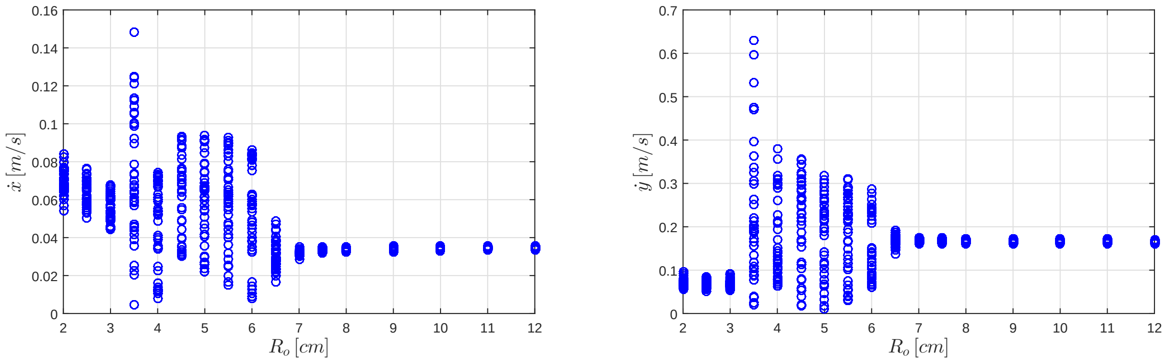

(a)

(b)

Figure 27: Sampled envelope's amplitude of the primary system velocity $\dot{x}$ (a) and the NES velocity $\dot{y}$ (b) are plotted as function of the distance R_o. Forcing: 0.6 m/s^2 - 6.2 Hz.

This section presents the numerical results illustrating the transition towards a chaotic behavior when the distance R_o gradually decreases. The simulations were performed for an amplitude and a frequency of the external forcing of 0.6 m/s and 6.2 Hz.

The sampled envelope's amplitude of the primary system velocity $\dot{x}$ (Fig. 27a) and the NES velocity $\dot{y}$ (Fig. 27b) are plotted as functions of the distance R_o. These plots represent two bifurcation diagrams for the system, as R_o is the varying parameter. It means that where several points exist for the same distance R_o, the envelope amplitude is not constant but varies during the time. We can observe that for a distance $R_o > 7$ cm the response is steady: i.e. the envelope has a constant amplitude. Between 6 and 7 cm there is the first bifurcation which brings to a periodic regime (6 cm). When R_o decreases further, the response is more and more non-deterministic until it appears to be steady again for $R_o < 3$ cm. This is caused by the fact that the two stable points in the bi-stable configuration gain stability as R_o gets smaller. The system ends up oscillating steadily around one of these two points.

7. Conclusions

In this paper the study of a new concept of nonlinear absorber with energy harvesting has been introduced and its experimental realization presented. The restoring force between the primary system and the NES is shaped thanks to an external magnetic force. The energy absorbed by the NES is converted into electrical energy by means of an electromagnetic transducer.

The results have shown that the presence of the magnetic force allows the NES to reach a purely cubic configuration by canceling out the linear term of the elastic force. The importance of having a purely nonlinear force between the NES and the primary system has been highlighted, since the presence of a linear component may radically change the response of the system. The Strongly Modulated Response seems to be a valid option in terms of energy absorption, suggesting that the nonlinearities may be used to improve the energy harvesting aspect. Interesting results leading to new open questions have arisen from the shaping of the force between the primary system and the NES via the magnetic force; particularly, the bistable configuration seems to be a promising path to follow.

This study unifies the research fields of nonlinear vibration absorbers and energy harvesting from vibrations showing the advantages of a combined application. An optimization process is still required in which the performances of the NES and the harvester would be investigated.

References

[1] O. Gendelman, Transition of energy to a nonlinear localized mode in a highly asymmetric system of two oscillators, Nonlinear Dynamics 25 (2001) 237–253.

[2] A. F. Vakakis, O. V. Gendelman, L. I. Manevitch, R. McCloskey, Energy pumping in nonlinear mechanical oscillators part ii – resonance capture, Journal of Applied Mechanics Transactions of the ASME 68 (2001) 42–48.

[3] A. Vakakis, O. Gendelman, L. Manevitch, R. McCloskey, Energy pumping in nonlinear mechanical oscillators i: dynamics of the underlying hamiltonian system, Journal of Applied Mechanics–Transactions of the ASME 68 (2001) 34–41.

[4] L. Manevitch, E. Gourdon, C. Lamarque, Parameters optimization for energy pumping in strongly nonhomogeneous 2 dof system, Chaos, Solitons and Fractals 31(4) (2007) 900–911.

[5] G. Kerschen, Y. S. Lee, A. F. Vakakis, D. M. McFarland, L. A. Bergman, Irreversible passive energy transfer in coupled oscillators with essential nonlinearity, SIAM Journal on Applied Mathematics 66(2) (2005) 648–679.

[6] D. McFarland, L. Bergman, A. Vakakis, Experimental study of non-linear energy pumping occurring at a single fast frequencyexperimental study of non-linear energy pumping occurring at a single fast frequency, International Journal of Non-Linear Mechanics 40(6) (2005) 891–899.

[7] E. Gourdon, N. Alexander, C. Taylor, C. Lamarque, S. Pernot, Nonlinear energy pumping under transient forcing with strongly nonlinear coupling: Theoretical and experimental results, Journal of Sound and Vibration 300(3) (2007) 522–551.

[8] G. Kerschen, J. Kowtko, D. McFarland, L. Bergman, A. Vakakis, Theoretical and experimental study of multimodal targeted energy transfer in a system of coupled oscillators, Nonlinear Dynamics 47(1) (2007) 285–309.

[9] Y. Starosvetsky, O. Gendelman, Strongly modulated response in forced 2dof oscillatory system with essential mass and potential asymmetry, Physica D 237(13) (2008) 1719–1733.

[10] E. Gourc, G. Michon, S. Seguy, A. Berlioz, Theoretical and experimental study of an harmonically forced vibro-impact nonlinear energy sink, Journal of Vibration and Acoustic 137 (2014) 031008.

[11] O. Gendelman, T. Bar, Bifurcations of self-excitation regimes in a van der pol oscillator with a nonlinear energy sink, Physica D 239(3) (2010) 220–229.

[12] Y. S. Lee, A. F. Vakakis, L. Bergman, D. McFarland, G. Kerschen, Suppressing aeroelastic instability using broadband passive targeted energy transfers, part 1: Theory, AIAA Journal 45(3) (2007) 693–711.

[13] Y. S. Lee, G. Kerschen, D. McFarland, W. J. Hill, C. Nichkawde, T. Strganac, L. Bergman, A. F. Vakakis, Suppressing aeroelastic instability using broadband passive targeted energy transfers, part 2: Experiments, AIAA Journal 45(10) (2007) 2391–2400.

[14] O. Gendelman, A. Vakakis, L. Bergman, D. McFarland, Asymptotic analysis of passive nonlinear suppression of aeroelastic instabilities of a rigid wing in subsonic flow, SIAM Journal on Applied Mathematics . 70(5) (2010) 1655–1677.

[15] B. Vaurigaud, L. Manevitch, C. Lamarque, Passive control of aeroelastic instability in a long span bridge model prone to coupled flutter using targeted energy transfer, Journal of Sound and Vibration 330(11) (2011) 2580–2595.

[16] O. Gendelman, Targeted energy transfer in systems with non-polynomial nonlinearity, Journal of Sound and Vibration 315 (2008) 732–745.

[17] O. Gendelman, C. Lamarque, Dynamics of linear oscillator coupled to strongly nonlinear attachment with multiple states of equilibrium, Chaos, Solitons and Fractals 24 (2005) 501–509.

[18] F. Georgiadis, A. F. Vakakis, D. M. McFarland, L. A. Bergman, Shock isolation through passive energy pumping caused by non-smooth nonlinearities, International Journal of Bifurcations and Chaos 15 (2005) 1–13.

[19] I. Karayannis, A. F. Vakakis, F. Georgiadis, Vibro-impact attachments as shock absorbers, Proceedings IMechE, Journal of Mechanical Engineering Science 222 (222) (2008) 1899–1908.

[20] Y. S. Lee, F. Nucera, A. F. Vakakis, D. M. McFarland, L. A. Bergman, Periodic orbits, damped transitions and targeted energy transfers in oscillators with vibro-impact attachments, Physica D 238 (2009) 1868–1896.

[21] F. Nucera, F. Lo Iacono, D. M. McFarland, L. A. Bergman, A. F. Vakakis, Application of broadband nonlinear targeted energy transfers for seismic mitigation of a shear frame: Part ii. experimental results, Journal of Sound and Vibration 313 (2008) 57–76.

[22] G. Pennisi, C. Stephan, E. Gourc, G. Michon, Experimental investigation and analytical description of a vibro-impact nes coupled to a single-degree-of-freedom linear oscillator harmonically forced, Nonlinear Dynamics 88 (2017) 1769–1784.

[23] S. P. Beeby, M. J. Tudor, N. M. White, Energy harvesting vibration sources for micro systems applications, Measurement Science and Technology 17 (2006) 175–195.

[24] P. Glynne-Jones, M. J. Tudor, S. P. Beeby, N. M. White, Anelectromagnetic, vibration-powered generator for intelligent sensor systems, Sensors and actuators A 110 (2004) 344–349.

[25] S. Roundy, P. K. Wright, J. M. Rabaey, Energy Scavenging for Wireless Sensor Networks, Springer NewYork, 2003.

[26] C. B. Williams, R. B. Yates, Analysis of a micro generator for microsystems, Proceedings of the 8th International Conference on Solid-state Sensors and Actuators Eurosensors IX (1995) 87–84.

[27] B. P. Mann, D. A. W. Barton, B. A. Owens, Uncertainty in performance for linear and nonlinear energy harvesting strate- uncertainty in performance for linear and nonlinear energy harvesting strategiesuncertainty in performance for linear and nonlinear energy harvesting strategies uncertainty in performance for linear and nonlinear energy harvesting strate, Journal of Intelligent Material Systems and Structures 23 (2012) 1448–1457.

[28] I. Sari, T. Balkan, H. Kulah, An electromagnetic micro power generator for wideband environmental vibrations, Sensors and Actuators A 145-146 (2008) 405–413.

[29] E. S. Leland, P. K. Wright, Resonance tuning of piezoelectric vibration energy scavenging generators using compressive axial load, Smart Material and Structures 15 (2006) 1413–1420.

[30] B. P. Mann, N. D. Sims, Energy harvesting from the nonlinear oscillations of magnetic levitation, Journal of Sound and Vibration 319 (2009) 515–530.

[31] S. Stanton, C. McGehee, B. P. Mann, Reversible hysteresis for broadband magnetopiezoelastic energy harvesting, Appl. Phys. Lett. 95 (174103).

[32] Z. Yang, Y. Zhu, J. Zu, Theoretical and experimental investigation of a nonlinear compressive-mode energy harvester with high power output under weak excitations, Smart Mater. Struct. 24.

[33] Y. Zhu, J. Zu, A magnetoelectric generator for energy harvesting from the vibration of magnetic levitation, IEEE transactions on magnetics 48.

[34] S. Stanton, C. McGehee, B. P. Mann, Nonlinear dynamics for broadband energy harvesting: Investigation of a bistable piezoelectric inertial generator, Physica D 239 (2010) 640–653.

[35] B. P. Mann, B. A. Owens, Investigations of a nonlinear energy harvester with a bistable potential well, Journal of Sound and Vibration 329 (2010) 1215–1226.

[36] K. Yung, P. Landecker, D. Villani, An analytical solution for the force between two magnetic dipoles, Magnetic and Electrical Separation 9 (1998) 39–52.

[37] E. Furlani, Permanent Magnet and Elecrtomechanical Devices, 1st Edition, Academic Press, New York, 2001.

[38] A. J. Sneller, B. P. Mann, On the nonlinear electromagnetic coupling between a coil and an oscillating magnet, J. Phys. D: Appl. Phys 43.